The Astronomical Journal, 155:170 (8pp), 2018 April https://doi.org/10.3847/1538-3881/aab14e

Surface Ice and Tholins on the Extreme Centaur 2012 DR_{30}

Gy. M. Szabó[1,2], Cs. Kiss[2], N. Pinilla-Alonso[3,4], E. Y. Hsiao[5], G. H. Marion[6], J. Györgyey Ries[6], R. Duffard[7], A. Alvarez-Candal[7,8,9], K. Sárneczky[2], and J. Vinkó[2,6,10]
[1] ELTE Eötvös Loránd University, Gothard Astrophysical Observatory, Szent Imre h. u. 112, Szombathely, Hungary
[2] Konkoly Observatory, Research Centre for Astronomy and Earth Sciences, Hungarian Academy of Sciences, Konkoly Thege 15-17, H-1121 Budapest, Hungary
[3] Department of Earth and Planetary Sciences, University of Tennessee, 1412 Circle Drive, Knoxville, TN 37996, USA
[4] Florida Space Institute, University of Central Florida, Orlando, FL, USA
[5] Department of Physics, Florida State University, Tallahassee, FL 32306, USA
[6] Department of Astronomy, University of Texas at Austin, 1 University Station C1400, Austin, TX 78712-0259, USA
[7] Instituto de Astrofísica de Andalucía-CSIC, Glorieta de la Astronomía s/n, E-18008 Granada, Spain
[8] European Southern Observatory, Alonso de Córdova 3107, Vitacura, Casilla 19001, Santiago 19, Chile
[9] Observatório Nacional, COAA, Rua General José Cristino 77, 20921-400 Rio de Janeiro, Brazil
[10] Department of Optics and Quantum Electronics, University of Szeged, Dm tr 9, H-6720 Szeged, Hungary
Received 2017 June 20; revised 2018 February 15; accepted 2018 February 19; published 2018 March 23

Abstract

2012 DR_{30} is one of the known solar system objects with the largest aphelion distance, exceeding 2200 au, on a high inclination orbit ($i = 78°$). It has been recognized to be either a borderline representative of high inclination, high perihelion distance (HiHq) objects, or even a new class of bodies, similar to HiHq objects for orbit but with an aphelion in the inner Oort Cloud. Here, we present photometry using long-term data from 2000 to 2013 taken by the SDSS sky survey, ESO MPG 2.2 m and McDonald 2.1 m telescopes, and a visual+near-infrared spectrum taken with the Southern Astrophysical Research Telescope and *Magellan* telescopes, providing insights into the surface composition of this body. Our best fit suggests that the surface contains 60% of complex organics (30% of Titan and 30% of Triton tholins) with a significant fraction of ice (30%, including pure water and water with inclusions of complex organics) and 10% silicates. The models also suggest a low limit of amorphous carbons, and hence the fragmentation of long-chained complex organics is slower than their rate of generation. 2012 DR_{30} just recently passed the perihelion, and the long-term photometry of the object suggested ambiguous signs of activity, since the long-term photometric scatter well exceeded the supposed measurement errors and the expected brightness variation related to rotation. Photometric colors put 2012 DR_{30} exactly between dark neutral and red objects, thus it either can be in a transition phase between the two classes or have differing surface properties from these populated classes.

Key words: Kuiper belt objects: individual (2012 DR30)

Supporting material: data behind figure

1. Introduction

According to our recent understanding of the outer solar system (e.g., Levison & Duncan 1997; Tiscareno & Malhotra 2003; Emel'yanenko et al. 2005; Di Sisto & Brunini 2007), Centaurs originated from the Kuiper Belt or the scattered disk by an ongoing migration of both the perihelion and the aphelion, and form the bridge between these trans-Neptunian objects (TNOs) and the Jupiter-family comets. This picture is disturbed by the existence of high inclination, high perihelion (HiHq, Brasser et al. 2012) objects, which can hardly be explained with an origin in the scattered disk. Brasser et al. (2012) estimate that the number of HiHq (q between 15 and 30 au, $i > 70°$, $Q < 100$ au) objects is not more than 200 down to 8 mag absolute brightness. To date, three such objects are known[11]; one of their first recognized representatives, 2008 KV_{42} even occupies a retrograde orbit. Two other HiHq-like objects are known (q between 15 and 30 au, $i > 70°$: 2002 XU_{93} and 2014 LM_{28}), with a $Q > 100$ au apastron distance. Their generally exotic orbits strongly suggest that they are originated directly from the Oort Cloud, and since their orbit is usually unstable, their presence in the current solar system may be evidence of a reservoir of HiHq objects in the Oort Cloud, which are occasionally scattered into inner orbits. Even so, there are arguments that the presence of HiHq objects is linked to the presence of an outer planetary-mass solar companion (Gomes et al. 2015).

2012 DR_{30} is a relatively recently discovered (MPEC 2012-D67) borderline HiHq object on a unique orbit, characterized by a high eccentricity of 0.9909, a high inclination of 78°. and a perihelion distance of 14.54 au. Its semimajor axis (1598.8 au) suggests that the aphelion (3183 au) is in the inner Oort Cloud (the epoch of orbital elements is 2017 September 4). The body of 2012 DR_{30} is 188 ± 9.4 km in diameter and has a relatively low V-band geometric albedo of $\approx 7.6^{+3.1}_{-2.5}$% using *Herschel* PACS and *WISE* observations (Kiss et al. 2013). A dynamical analysis of the target's orbit shows that 2012 DR_{30} moves on a relatively unstable orbit and was most likely only recently placed on its current orbit from the most distant and still highly unexplored regions of the solar system (Kiss et al. 2013).

2012 DR_{30} spends 98.5% of time outside the heliosphere (at distances indicatively >100 au from the Sun), also avoiding the heliotail (McComas et al. 2013). In this environment, solar irradiation is negligible and there is no solar wind, but a significantly slower interstellar gas flow is observed, mostly in the form of interstellar neutral hydrogen ($T \approx 10^4$ K, 26 km s^{-1}) that is partially ionized by the solar UV irradiation.

[11] JPL Small-body Database Search Engine, ssd.jpl.nasa.gov/sbdb_query.cgi.

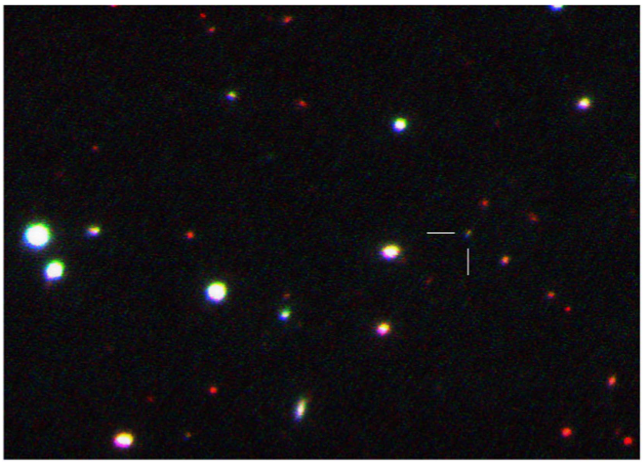

Figure 1. Prediscovery image of 2012 DR_{30} (marked in the right half of the image) on the SDSS frame taken on 2000 April 5, 6:16 TAI.

There is also a high-energy cosmic-ray irradiation present (Dartois et al. 2013).

2012 DR_{30} is a prime representative of several open questions concerning the distant solar system. Its Tisserand parameter of $T_J = 0.198$ classifies 2012 DR_{30} as a Damocloid (Jewitt 2005), which are thought to be inactive Halley-type or long-period comets. However, the orbital elements do not closely resemble a Damocloid, which has a median a and q of 19.6 and 2.38 au, respectively. Only one Damocloid exceeds the perihelion distance of 15 au, the HiHq object 2008 KV_{42} that is sometimes dubbed as the "outer Damocloid."

The observed albedo of ≈8% is brighter than typical Damocloids exhibit (Fernández et al. 2005), and also exceeds that of extinct/dormant periodic comets (Lamy et al. 2004), but still may suggest a processed surface. Rabinowitz et al. (2013) noted that the HiHq 2010 WG_9 is similar to 2012 DR_{30} in surface colors, aphelion distance, and inclination. On the other hand, 2010 WG_9 is a suspected binary of components with different composition, and therefore its color does not correspond to a unique body.

Thus, the key to the real nature of 2012 DR_{30} lies in the surface composition and properties that will classify the object into a group of other well-known solar system objects. From photometry, it was suggested earlier that the spectrum is flat and proves a low albedo, which is similar to blue Centaurs or Trojans (Kiss et al. 2013). From photometry, a feature was suspected around the Z band, but this has not been confirmed. In order to uncover the spectral properties and the surface composition, we present here an analysis of the visible and near-infrared (0.4–2.3 μm) spectrum of 2012 DR_{30}. Further photometry was also taken to monitor the long-term behavior of the absolute brightness and to observe the evolution of colors and to reveal possible brightening as signals of low-level cometary activity while getting closer to the Sun.

2. Observations and Data Reduction

2.1. Photometry

SDSS observed 2012 DR_{30} two times in the spring of 2000 (2000 March 30, April 5; Figure 1), well before the discovery of this TNO and the other HiHq objects. From these sets of images, the second run had enough S/N to measure the flux of 2012 DR_{30} (in the g, r, and i bands); the first one from March 30 was of significantly poorer quality. Due to the slow motion of 2012 DR_{30}, the detections were missed by the Moving Object Catalog (SDSS MOC; e.g., Ivezić et al. 2002), but we could identify the observations with the Solar System Object Image Search tool of the Canadian Astronomy Data Center.[12] On the same website, there is a suspicious report about a Southern Astrophysical Research Telescope (SOAR) observation from 2010, but in that case, the TNO was just outside the image and had not been observed.

Table 1
Log of Photometric Observations Included in the Present Analysis

Date	Obs	R (au)	Δ (au)	α	Filter (s)	Exp
2000 Apr 05	SDSS	22.44	22.12	2.4	g	1 × 53
2000 Apr 05	SDSS	22.44	22.12	2.4	r	1 × 53
2000 Apr 05	SDSS	22.44	22.12	2.4	i	1 × 53
2012 Jun 06	ESO MPG[a]	14.68	14.70	3.9	V	3 × 60
2012 Jun 06	ESO MPG[a]	14.68	14.70	3.9	R	3 × 60
2012 Jun 06	ESO MPG[a]	14.68	14.70	3.9	I	3 × 60
2013 Mar 23	McD	14.91	14.10	2.4	r	160
2013 Mar 23	McD	14.91	14.10	2.4	i	160
2013 Apr 13	McD	14.93	14.26	2.7	r	300
2013 Apr 13	McD	14.93	14.26	2.7	i	300
2013 Apr 13	McD	14.93	14.26	2.7	z	300

Note.
[a] Kiss et al. (2013).

We also included here the *VRI* images taken with the ESO MPG on 2012 June 6 (Kiss et al. 2013) in the present analysis. More *ri* and *griz* images were taken from the McDonald Observatory on 2013 March 23 and April 13. The McDonald Observatory images were obtained using a South Korean guest instrument, CQUEAN, with a 0.″28 $pixel^{-1}$ resolution and with a 4.′8 × 4.′8 field of view. The instrument is optimized for the red wavelength, with the best and strongest image in i. We guided on stars, which resulted in 0.″4 and 0.″7 trails for the object. The estimated seeing was around 1.″2 in i at zenith on both nights. However, the minimum Zenith distance of the object was larger than 63° from McDonald at the time of the observations, resulting in larger point spread functions (PSFs) in every filter.

The log of photometric observations is summarized in Table 1.

2.2. Spectroscopy

The visible spectrum of 2012 DR_{30} has been observed in service mode using the Goodman HT Spectrograph installed at the 4.1 m SOAR in Cerro Pachón, Chile. The Goodman HT Spectrograph was used in single long slit mode, with a slit of 1.″03 in width. It was equipped with a blocking filter GG-385 and a grating of 300 line/mm, which gives a resolution $R \approx 1390$. This configuration gives a spectrum ranging from 0.32 to 0.85 μm. SA102-1081 used as a telluric and solar analog, observed at an airmass of 1.18 (the airmass of 2012 DR_{30} was 1.05) and with a 5 s exposure time. Data were reduced using standard IRAF techniques, and were wavelength calibrated using HgAr lamps. The spectra of 2012 DR_{30} were then divided by the solar analog spectra.

[12] http://www3.cadc-ccda.hia-iha.nrc-cnrc.gc.ca/en/ssois/

Table 2
Log of Spectroscopic Observations

Date	UT	R (au)	Δ (au)	Airmass
2013 Feb 13	18:25:49	14.87	14.12	1.05
2013 Mar 25	03:14:05	14.91	14.11	1.01

Wavelength region (μm)	Resolution	Exposure time (s)	S/N
0.32–0.85	1390	1 × 1600	50
0.8–2.5	500	8 × 158.5	32

A spectrum covering the near-infrared region between 0.8 and 2.5 μm was obtained on March 25.135 UT with the FoldedPort Infrared Echellette (FIRE) spectrograph on the 6.5 m *Magellan* Baade Telescope at Las Campanas Observatory, Chile. The data were taken in the low-resolution prism mode ($R \approx 500$ in the J band) with the standard 0.6 arcsec slit width. An A0V-type star HD105992 was the telluric and flux standard for the NIR spectrum. The airmass for the standard was 1.03, and the airmass for the science target was 1.01; both the standard star and the science target were taken at a parallactic angle. Irradiance correction consisted of dividing by a model spectrum with solar parameters, taken from the library of Munari et al. (2005). This model spectrum is a suitable representative of the solar irradiation, making use of the widely trusted ATLAS9 models (e.g., Castelli & Kurucz 2004 and references therein), and no significant biases are expected due to this step. Additional details on the spectroscopic observation can be found in Table 2. Data reduction was performed by applying customized IDL routines.

VIS and NIR spectra do not overlap in wavelength range. In order to join both spectra we fit a straight line to the visible spectrum and extend it to cover the longer wavelengths up to 1.1 μm. Then we used this continuum model and the NIR spectrum between 1 and 1.1 μm to merge them. Being taken at different epochs, the two parts of the spectrum likely do not cover the same region on the surface. Although previous observations of 2012 DR_{30} (Kiss et al. 2013) do not detect any color variation, we cannot discard the possibility of some change in the slope due to different materials on the surface. Based on the dispersion in the R and I colors shown in Figure 3, we estimate that the difference in the slope would be of $<8\%$.

3. Results and Analysis

3.1. Photometry

Due to the several sources with different filter systems of photometric data, magnitudes and color indices were converted to the widely accepted values of standard magnitudes and illumination corrected colors. A standard X magnitude of a kind $X(1, 1, \alpha)$ is determined as $X - 5\log(R\Delta)$, where X is the measured value after standard photometric calibrations, and R and Δ are the heliocentric and geocentric distances. Here, we do not apply a correction for the α phase angle because the coefficients cannot be fitted reliably from the current data, but since the solar phase of 2012 DR_{30} was always between $2\overset{\circ}{.}4$ and $3\overset{\circ}{.}9$ during the observations, and the coefficients for TNOs and comets are typically found in the range of 0.05–0.08 mag $\deg^{-1}$ around the 3° phase angle, neglecting that the phase variations will not introduce larger biases

Table 3
Absolute Magnitudes and Colors of 2012 DR_{30}

Date	Filter	AB mag	Color
2000 Apr 05	$r(1, 1, \alpha)$	$7\overset{m}{.}70(9)$	
2000 Apr 05	$(g - r) - (g - r)_\odot$		$0\overset{m}{.}11(14)$
2000 Apr 05	$(r - i) - (r - i)_\odot$		$0\overset{m}{.}26(11)$
2012 Jun 06	$r(1, 1, \alpha)_{synth}$[a]	$7\overset{m}{.}40(3)$	
2012 Jun 06	$(V - R) - (V - R)_\odot$		$0\overset{m}{.}15(4)$
2012 Jun 06	$(R - I) - (R - I)_\odot$		$0\overset{m}{.}08(4)$
2013 Mar 23	$r(1, 1, \alpha)$	$7\overset{m}{.}22(8)$	
2013 Mar 23	$(r - i) - (r - i)_\odot$		$0\overset{m}{.}30(12)$
2013 Apr 13	$r(1, 1, \alpha)$	$7\overset{m}{.}63(5)$	
2013 Apr 13	$(g - r) - (g - r)_\odot$		$0\overset{m}{.}05(10)$
2013 Apr 13	$(r - i) - (r - i)_\odot$		$0\overset{m}{.}53(3)$

Note. Note that magnitudes are converted to the ab system, while colors are corrected to the solar values. The errors in the last digits are given in parentheses.
[a] Synthesized r magnitude ($r = V - 0.42(B - V) + 0.11$), according to Jester et al. (2005).

to the reduced magnitudes as $0\overset{m}{.}1$. The observed colors were corrected to the solar illumination, leading to $(g - r) - (g - r)_\odot$ and analogous indices. We include the resulting colors in Table 3.

The absolute $r(1, 1, \alpha)$ brightnesses of 2012 DR_{30} were consistent with values between $7\overset{m}{.}2$ and $7\overset{m}{.}7$. However, the scatter of photometric points is definitely above the photometric errors: the suspected brightness and color variations have a standard deviation of $0\overset{m}{.}21$ and $0\overset{m}{.}18$, respectively. No correlation is observed with the phase angle (Pearson's $r = 0.21$). A similar finding can usually be straightforwardly explained by the rotation of a non-spherical body, which could cause a brightness change of several tenths of magnitudes. However, Kiss et al. (2013) gave evidence for a very little brightness variation of 2012 DR_{30}, so in the case of this particular object, the scatter in the photometry is likely not of rotational origin.

The long-period light variations of 2012 DR_{30} (as it was observed in the R and r bands only) somewhat resemble that of Chiron (e.g., Duffard et al. 2002), where the amplitude of light variations can get close to 1 mag, as their data set in the mid-2000s shows. The light variation of Chiron was first detected in 1978 and suggested as a possible indicator of activity, but the coma was not imaged before the observation of Meech & Belton (1989). In the case of DR_{30}, the simplest way to explain the brightness variations would be a similar cometary activity, but due to the faintness of the object and the S/N ratio of our images, the coma has not been seen directly.

A counterargument for the suspected activity is the observed color variation. $V - R$ and the somewhat similar $g - r$ colors are stable between $0\overset{m}{.}05$ and $0\overset{m}{.}15$ for all observations, but $r - i$ and $R - I$ colors scatter a lot in the range of $0\overset{m}{.}1$–$0\overset{m}{.}5$, with a median value of $0\overset{m}{.}28$, and no correlation with the phase angle. This feature could be linked to colored spots on the surface that can evolve in the presence of irradiation. Albedo variegation due to colored surface spots is known for main-belt asteroids and also TNOs (e.g., Lacerda et al. 2008), and also found to be present on many main-belt asteroids at smaller level (Szabó et al. 2004). However, in the case of 2012 DR_{30}, albedo variegation is unlikely because it would emerge in brightness variations related to the rotation, well above the upper limit derived by of Kiss et al. (2013).

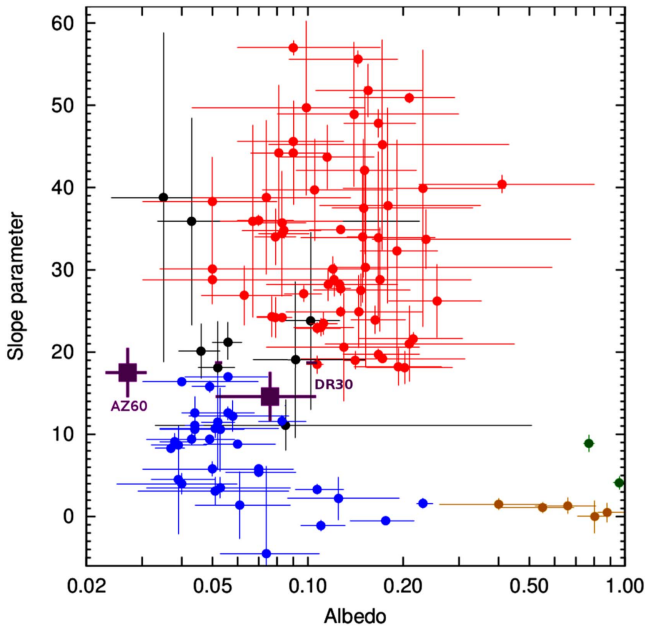

Figure 2. Slope parameter vs. albedo relations for 111 TNOs, including 2012 DR_{30} and 2013 AZ_{60} on the color–albedo diagram of TNOs (Lacerda et al. 2014). 2012 DR_{30} is exactly between the dark neutral objects (blue points) and bright red objects (red points). Black points show objects with large uncertainties and ambiguous surface type. Large TNOs (green) and objects with Haumea-type surfaces (orange) occupy a third group (bottom right).

From the current data, one can only propose some concepts that can explain the light variations in the r and R bands and the far-end color, but without leading to rotational light variation exceeding the limit found by Kiss et al. (2013). A temporary atmosphere can lead to frost formation on large bodies such as Hale–Bopp (Szabó et al. 2012), which can explain changes in brightness and color, but not cause colored spots on the surface. There is of course no firm proof on this or a similar scenario in the current data, and the explanation can only be expected from further photometry and imaging.

The position of 2012 DR_{30} in the slope–albedo diagram is shown in Figure 2, in comparison with other TNOs in the literature. 2012 DR_{30} is on the edge of the dark neutral objects close to the large group of bright red objects as defined by Lacerda et al. (2014). This can either signify a transient object between the two classes, e.g., it was bright and red, and now the surface is under darkening and losing the color. In this case, the surface composition reflects the processes of this transition between the two main classes. The other possibility is that 2012 DR_{30} stably exhibits the observed spectral features, and it is a special example of the dark neutral group. Interestingly, in addition to some Centaurs and scattered disk objects in the transition region between the two groups, some irregular satellites of the giant planets also exhibit similar color–albedo properties (see Farkas-Takács et al. 2017 and references therein) with similar heliocentric distances to the perihelion distance of 2012 DR_{30}.

3.2. Spectroscopy

The normalized VIS+NIR spectrum is shown in Figure 3. The spectrum of 2012 DR_{30} is red and featureless in the visible and up to 1.9 μm. The slope is consistent with color indices of $(g-r)-(g-r)_\odot = 0\overset{m}{.}18$ and $(r-i)-(r-i)_\odot = 0\overset{m}{.}14$.

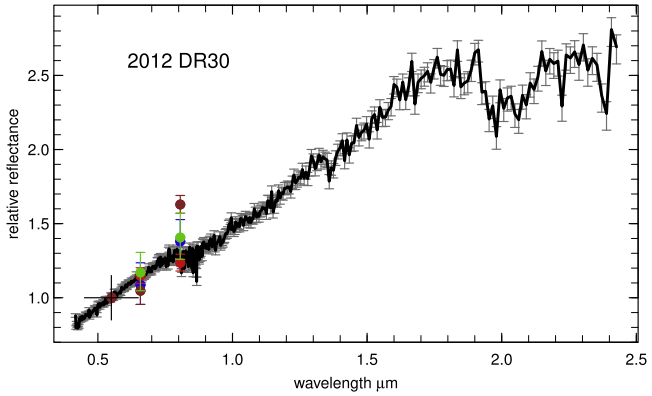

Figure 3. Observed VIS+NIR spectrum of 2012 DR_{30}, normalized at 550 nm. Photometric data are shown with filled symbols: blue, 2000 April 5; red, 2012 June 6; green, 2013 March 23; brown, 20013 April 13. (The data used to create this figure are available.)

Here, $g-r$ is redder than any of the photometric measurements and $r-i$ close to the bluest extremities, but the general slope is consistent with the photometric color indices. There is a clear absorption at 2.0 μm. This absorption is typically attributed to the presence of water ice on the surface of the objects. Water ice also causes another absorption band near 1.52 μm; however, we do not detect any other absorption in our spectrum above the noise. This is not new; there are other TNOs or Centaurs that show only the strongest absorption of water ice in the NIR, for example, Lorenzi et al. (2014) estimate 25% of water ice on the surface of Varuna and they do not detect an absorption at 1.5 μm.

To compare our spectrum with other red spectra in the literature we compute the slope parameter (Luu 1993) of the continuum between 0.4 and 1.7 μm. The normalized reflectivity gradient is $S' = 14.5\%/1000$ Å. The precision, i.e., the standard deviation of the slope parameter is 0.05%, but considering the usual systematics, the derived slope is accurate to ≈1%. We also estimate the depth of the water-ice band at ≈2.0 μm as $D: = (1-R_b)/R_c = 0.12 \pm 0.01$, where R_b is the reflectance in the center of the band and R_c is the reflectance of the continuum in the same wavelength calculated with a linear fit to the right and left sides of the band.

In Figure 4, we compare the spectrum of 2012 DR_{30} with the spectrum of other objects representative of different dynamical populations. This figure shows that the optical slope parameter of 2012 DR_{30} is redder than most of the comparison objects, but not as red as the red Centaurs (which have a slope parameter between 27% and 48%; Duffard et al. 2014), represented in this figure by Pholus. The spectrum also differs from that of a blue or red Trojan. This comparison and the shape of the spectrum of 2012 DR_{30} suggest that this is an irradiated surface composed of complex organic material with some amount of water ice. Other similar surfaces can also contain a certain amount of amorphous silicates. When we compare the spectrum with other similar objects (Figure 4), we find that it is more similar to the gray Centaurs (e.g., Thereus, a gray Centaur with water ice, or the retrograde Centaur 2008 YB_3) than to the red Centaurs such as Pholus (gray Centaurs have a slope ranging from −1% to 17%; Duffard et al. 2014). In the next section we model the spectrum of this object to better understand its surface composition.

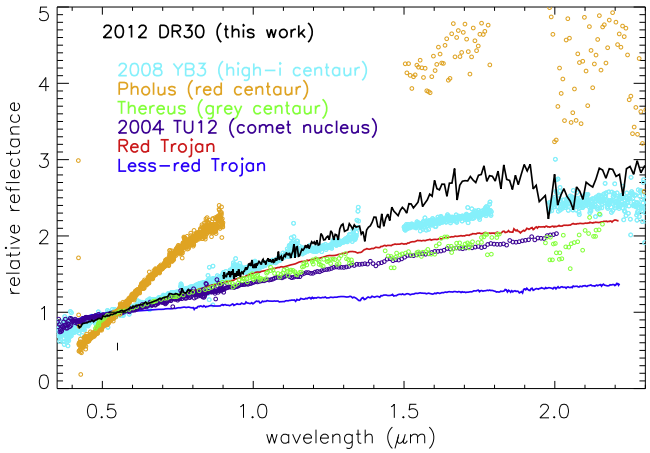

Figure 4. Comparison of the spectrum of 2012 DR_{30} and some other primitive minor bodies available in the literature (following Pinilla-Alonso et al. 2013): a red Centaur, Pholus (Fornasier et al. 2009; Perna et al. 2010; Barucci et al. 2011); a gray Centaur, Thereus (Licandro & Pinilla-Alonso 2005); the average spectrum of the red and gray Trojans (Emery et al. 2011); the spectrum of 2004 TU_{12}, a red comet nucleus (Campins et al. 2006).

3.3. Modeling of the Spectrum

Fitting reflectance spectra of TNOs and Centaurs with synthetic spectra is an effective tool to study the surface composition of these objects (Hapke 1993 and references therein; Shkuratov et al. 1999). These methods have been widely used, leading to important discoveries in the understanding of the surfaces of minor bodies, e.g., the first discovery of water ice and organics on the surface of asteroid 24 Themis (Campins et al. 2010), the characterization of the first family of TNOs (Pinilla-Alonso et al. 2007, 2009) or, more recently, the study of the surface of Pluto through modeling of *New Horizons* spectra (Protopapa et al. 2017).

In the modeling efforts, the grain sizes and relative abundances of candidate materials are adjusted iteratively to minimize the differences between the resulting synthetic albedos and the observations. In this work, we have used the Shkuratov method to obtain the reflectance of a surface composed of a maximum of five ingredients mixed intimately (also known as "salt and pepper" mixture). We follow a similar approach that was used previously by our group for other minor icy objects (Duffard et al. 2014; Lorenzi et al. 2014). In a first step, we ran models using different materials that have been previously proposed as part of the surface of other TNOs. We included amorphous and crystalline water ice in pure form and with tholin inclusions (Mastrapa et al. 2009), amorphous pyroxenes and olivine with different relative ratios of Mg/Fe (Dorschner et al. 1995), titan tholin (Khare et al. 1984), triton tholin (McDonald et al. 1994), amorphous carbon (AC; Rouleau & Martin 1991), kerogen (Khare et al. 1990), and methanol (J. Emery 2018, personal communication).

We show the comparison of the reflectance of some individual components tested in this step and the observed comet spectrum in Figure 5. The components that we are going to use in the next step are drawn with solid lines, while the ones that were omitted from the final fit are drawn with dashed lines (see the caption for the list of the components). The model spectra show different kind of homogeneous surfaces, assuming that pure material is present in the form of 20 μm sized particles. In the case of methanol, we plot the reflectance spectrum based on the laboratory measurement of a 13.7 μm thick layer, published in Cruikshank et al. (1998). Of course these curves are not considered as template patterns during the fitting procedure, where the spectrum of the mixture with variable compositions and grain sizes were calculated exactly. But this comparison gives a hint about the prominent spectrum shape and specific features due to the different components, and for example, nicely illustrates the presence of the water band (around 2 μm) in the spectrum. For example, carbon and kerogen behave similarly, they show a featureless curve with moderate red slope and low albedo, both are discarded for the final step. Methanol ice has been used before to model Pholus and there are hints of its presence on a small number of TNOs in the RR class, the most diagnostic feature when it comes to TNOs surface composition is the band at 2.27 μm (Brunetto et al. 2006; Barucci et al. 2011). Methanol is also discarded in the first step of our modeling. This is consistent with our observations as we do not detect this absorption band (see Figure 3). Also, the slope of 2012 DR_{30} corresponds to a TNO in the BR class, not the RR class.

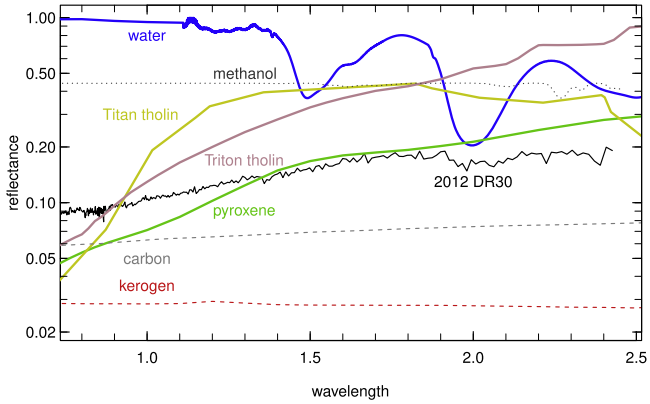

Figure 5. Comparison of materials considered in the modeling. The spectrum is shown by the black line, while sample spectra of different bodies with arbitrary material parameters are: water—blue line, Titan tholin—yellow line, Triton tholin—pink line, piroxene—green line, carbon—gray dashed line, kerogen—red dashed line, methanol—magenta dashed line. Materials plotted with solid line took part in the best fit.

Table 4
Details of the Materials Used in the Best-fit Model of 2012 DR_{30}

Material	Reference
Amorphous Water Ice	Mastrapa et al. (2009)
Amorphous pyroxene (Mg_x $Fe_{1-x}SiO_3$ ($x = 0.7$))	Dorschner et al. (1995)
Titan Tholin	Khare et al. (1984)
Triton Tholin	McDonald et al. (1994)

After running many combinations of materials, relative abundances, and particle sizes, our modeling selects the components that provide the best fits based on the value of the reduced χ^2. We found that the best fits come from a mixture of five ingredients (see Table 4 for the details of the optical constants): amorphous water ice; amorphous pyroxene (with a low amount of iron, 30%); Triton tholin; Titan tholin and amorphous water ice with fine inclusions of Triton tholins (the size of the inclusions is much smaller than the size of the water ice particles) accounting for the 12% of the volume of water ice (hereafter "water with inclusions").

As a second step, we calculated a grid of models varying the relative abundances and the particle sizes of the accepted

Table 5
Space of Parameters where we Look for the Best Fit to The Relative Reflectance of 2012 DR_{30}

Material	Abundance	Particle Size (μm)
Water Ice With Inclusions	0–60	8–40
Water Ice (amorphous)	0–110	5–37
Titan Tholin	0–40	150–3450
Triton Tholin	0–50	8–28
Pyroxene	0–40	10–110

materials (see Table 5 for the range of variation of these variables covered in this step). Our modeling considers the possibility of 0% of abundance of one or more materials, so the final number of components in the surface will be determined by the modeling. We selected from these models those which were consistent with 7.5%–9.2% visible albedo (Kiss et al. 2013), and we ranked them using the reduced χ^2 value.

From the grid of models we selected the models that have at least 90% confidence, a total of 62 models. This statistically selected sample provides constraints for the values of the relative abundances and the particle sizes. In the last step, we proceed with the visual confirmation of the collection of 62 models. Fortunately, the shape of the spectrum of 2012 DR_{30} is peculiar and its characteristics (i.e., red slope in the visible, clear absorption at 2.0 m, and lack of absorption at 1.52 m) resulted in good sensitivity in defining the acceptable model compositions of the quite limited number of components we involved in the final modeling step.

In Figures 6 and 7, we show the collection of 18 synthetic models that best reproduce the spectrum of 2012 DR_{30} together with the one that we prefer as "best fit." In the plot we normalized each synthetic albedo and the spectrum to unite at 0.7 μm. This is better to show the variation allowed for the albedo at 0.55 μm, based on the estimated optical albedo by Kiss et al. (2013). The space of parameters covered by these models are presented in Figure 7. The characteristics of the best fit are detailed in Table 6.

We examined the degenerations in the parameter space, which is tolerable and supports the stability of the best-fit solution (Table 7). The most important degenerations emerge between the two water-ice components (pure ice and ice with inclusions), and also pyroxene and Triton tholin. The two water-ice components together sum up to 30% in the best fits, hence the total water content is well determined. The identified correlation between pyroxene and Triton tholin is most likely due to the similar spectral shape of these components (Figure 5), which may make them mathematically similar, but their difference in albedo enables us to conclude on a lower amount of pyroxene and larger amount of Triton tholin in the fitting procedure: in all of the best models, the modeled amount of Triton tholin well exceeded the modeled amount of pyroxene. In summary, the results are based on our initial assumptions including a limited set of different chemical compounds, but we could get a rough picture on the composition.

4. Discussion

Our solutions give very good constraints of the relative amount of each material in the mixture. According to our collection, the surface is composed of 40%–60% of complex organics (Titan and Triton tholins, with 60% being the most

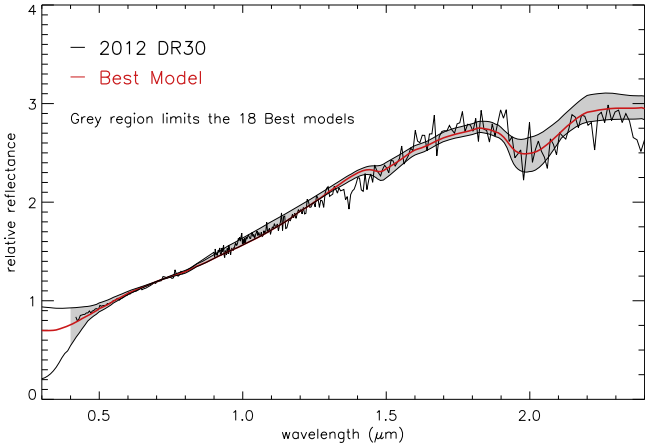

Figure 6. Best-fit solution plotted against the observed spectrum. The shaded region shows the area covered by the 18 best-fit solutions.

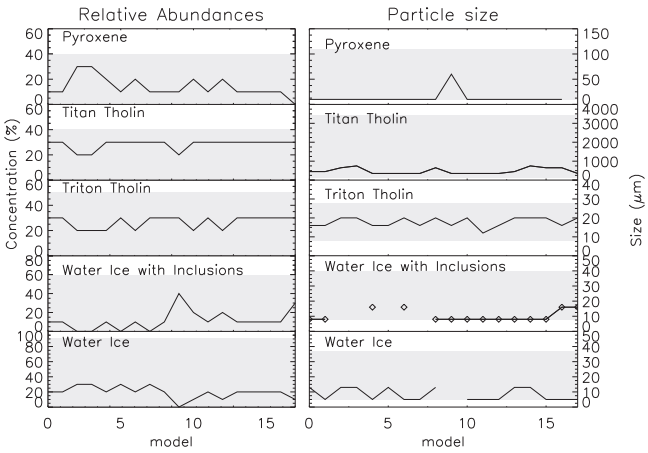

Figure 7. The 18 best-fit models in the parameter space. Shaded regions show the allowed range of the parameters, while the line connects the resulted fraction and grain size of the models in the consecutive fits.

Table 6
Best Fit to the Relative Reflectance of 2012 DR_{30}

Material	Abundance	Particle Size (μm)
Water Ice With Inclusions	10 (0–20)	16
Water Ice (amorphous)	20 (10–20)	5
Titan tholin	30 (10–30)	350
Triton tholin	30 (20–30)	20
Pyroxene	20 (10–30)	10
All Water	30 (30)	...
All Tholins	60 (40–60)	...
Pyroxene	10 (10–30)	...
Albedo	7.8%	...

Note. See the range of parameters covered by the 18 best fits in parentheses

Table 7
Correlation Matrix of Fit Parameters

	Water Ice Inclusions	Water	Pyrox.	Titan	Triton
Ice & Inc.	1	0.8	0.1	0.6	−0.1
Water		1	0.3	0.6	−0.2
Pyroxene	...	...	1	0.1	0.8
Titan	...	...	...	1	0.1

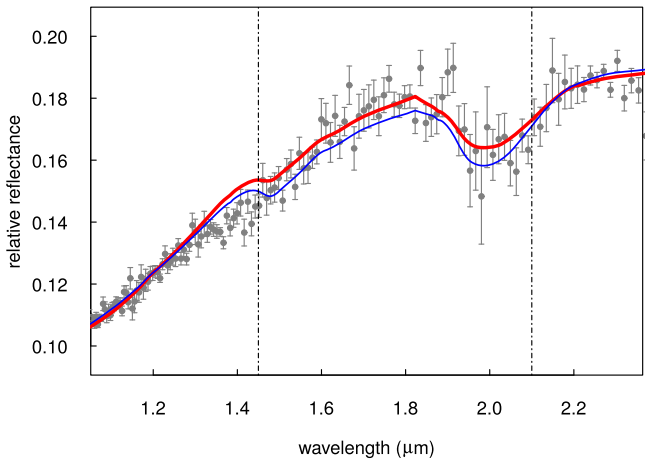

Figure 8. Illustration of low surface AC ratio. Red and blue curves plot fits assuming 0% and 12% surface AC, respectively. See further discussion in the text.

preferred value), 30% of water ice (including that with and without inclusions), and 10%–30% of pyroxenes (with 10% being the most preferred value). Inclusions of complex organics (in this case Triton tholin) are present in most of the solutions, which helps to fit the shape of the continuum in the visible. (The amount of pure water ice varies from 10% to 30% and the amount of water with inclusions from 0% to 20%, but the total amount of water, considering both components, is always 30%.) The red color, the absorption features, and the low albedo of 2012 DR_{30} are well matched by a surface composition rich in dark complex organics intimately mixed with water ice and with a lower amount of amorphous silicates.

The size of the particles is also well constrained by our solutions, and the surface of 2012 DR_{30} is formed mostly by small particles with sizes ≈10–50 μm, except for the Titan Tholin whose size is in the range of the 300–2000 μm. The presence of water ice on the surface of 2012 DR_{30} is consistent with having a visible albedo higher than the typical albedo of Damocloids and extinct/dormant comets, where the surface is composed of a mantle of processed materials covering the ices.

We tested the non-presence of AC on the surface. Amorphous carbon (AC) is the end state of the irradiation of simple organics (CH_4, CH_3OH) that under the influence of ion irradiation become darker (Andronico et al. 1987). AC has commonly been used to model the spectra of different TNOs and Centaurs (e.g., Pholus: 60%—Cruikshank et al. 1998; Thereus: 40%—Licandro & Pinilla-Alonso 2005; Varuna: 15%—Lorenzi et al. 2014; Chariklo: 60%–70%—Duffard et al. 2014; and AC was required to model the TNOs in the sample in Guilbert et al. 2009). Therefore, it was surprising that the initial tests had shown that ACs are not required for modeling the 2012 DR_{30} spectrum.

To test the non-detection of ACs, we observed test runs with the detected components and all these components plus ACs, and compared the rms value of the best fits. We performed a random walk optimization from 1000 randomized starting points, consisting of 2000 steps in each sequence. We found that the presence of ACs resulted to be very low, at most a few percent on the surface. An illustration is plotted in Figure 8, where we compare the best fit without AC (red curve), and the best fit if 12% AC is forced on the surface (blue curve). The best fits are identical in the visual range (which we do not plot here), the important difference emerges between 1.35 and 2.1 μm. Here, the peak at around 1.8 μm is reproduced only if no carbon is assumed (reduced $\chi^2 = 1.2$), while with increasing AC ratio, this peak gets fainter and the fit is significantly worsened (reduced $\chi^2 = 1.6$, suggesting a <10% upper limit of AC components). Note that the observed spectrum is supposed to suffer biases due to a band of telluric lines at around 1.4 μm. Since we wanted to avoid misinterpreting the possible biases in this region, we limited the short-wavelength end of the tested range at 1.45 um.

The apparent low amount of AC on 2012 DR_{30} may have significant implications on understanding the formation of complex organics on its surface. We cannot estimate the formation and lifetime of the tholins observed on DR_{30}, but we can speculate that their decomposition seems to be significantly slower than their formation, leading to a lack of ACs. The origin of organic matter on Earth has been debated for a long time, invoking terrestrial abiogenesis and impact of comets and asteroids of the inner solar system. Since 2012 DR_{30} is highly enriched in tholins, with a suspected low rate of ongoing decomposition, this body may be a messenger from a distant, reasonably large reservoir of organic matter in the Oort Cloud. However, as indicated by its color and albedo, 2012 DR_{30} is different from the bulk of distant objects (>40 au) and it may get its observable surface composition during those short periods when it is close to its heliocentric passage.

The research leading to these results have been supported by the the Hungarian National Research, Development and Innovation Office (NKFIH) grants K-115709, K-119517, K-125015, PD-116175, and the GINOP-2.3.2-15-2016-00003, the European Unions Horizon 2020 Research and Innovation Program, under Grant Agreement No. 687378 (Small Bodies: Near and Far) and the Lendület LP2012-31 and LP2014-17 grants of the Hungarian Academy of Sciences, and by the City of Szombathely under agreement No. S-11-1027. L.M. was supported by the János Bolyai Research Scholarship of the Hungarian Academy of Sciences.

E.Y.H. acknowledges the support provided by the National Science Foundation under grant Nos. AST-1008343 and AST-1613472. E.H. and G.H.M. acknowledge the excellent support provided by the staff of the Las Campanas Observatory during the FIRE observations. J.G.R. and J.V. are grateful for the granted telescope time on the 2.1 m Otto Struve telescope at McDonald Observatory. R.D. acknowledges the support of MINECO for his Ramón y Cajal Contract. A.A.C. acknowledges support from the Marie Curie Actions of the European Commission (FP7-COFUND), FAPERJ, and CNPq.

This paper includes data gathered with the 6.5 meter *Magellan* Telescopes located at Las Campanas Observatory, Chile. We acknowledge the Southern Astrophysical Research (SOAR) telescope, which is a joint project of the Ministerio da Ciencia, Tecnologia, e Inovacao (MCTI) da Republica Federativa do Brasil, the U.S. National Optical Astronomy Observatory (NOAO), the University of North Carolina at Chapel Hill (UNC), and Michigan State University (MSU).

ORCID iDs

Gy. M. Szabó https://orcid.org/0000-0002-0606-7930
Cs. Kiss https://orcid.org/0000-0002-8722-6875
N. Pinilla-Alonso https://orcid.org/0000-0002-2770-7896
E. Y. Hsiao https://orcid.org/0000-0003-1039-2928
J. Györgyey Ries https://orcid.org/0000-0002-9825-2550

R. Duffard https://orcid.org/0000-0001-5963-5850
A. Alvarez-Candal https://orcid.org/0000-0002-5045-9675
K. Sárneczky https://orcid.org/0000-0003-0926-3950
J. Vinkó https://orcid.org/0000-0001-8764-7832

References

Andronico, G., Baratta, G. A., Spinella, F., & Strazzulla, G. 1987, A&A, 184, 333
Barucci, M. A., Alvarez-Candal, A., Merlin, F., et al. 2011, Icar, 214, 297
Brasser, R., Schwamb, M. E., Lykawka, P. S., & Gomes, R. S. 2012, MNRAS, 420, 3396
Brunetto, R., Barucci, M. A., Dotto, E., & Strazzulla, G. 2006, ApJ, 644, 646
Campins, H., Hargrove, K., Pinilla-Alonso, N., et al. 2010, Natur, 464, 1320
Campins, H., Ziffer, J., Licandro, J., et al. 2006, AJ, 132, 1346
Castelli, F., & Kurucz, R. L. 2004, A&A, 419, 725
Cruikshank, D. P., Roush, T. L., Bartholomew, M. J., et al. 1998, Icar, 135, 389
Dartois, E., Ding, J. J., de Barros, A. L. F., et al. 2013, A&A, 557, AA97
Di Sisto, R. P., & Brunini, A. 2007, Icar, 190, 224
Dorschner, J., Begemann, B., Henning, T., Jaeger, C., & Mutschke, H. 1995, A&A, 300, 503
Duffard, R., Lazzaro, D., Pinto, S., et al. 2002, Icar, 160, 44
Duffard, R., Pinilla-Alonso, N., Ortiz, J. L., et al. 2014, A&A, 568, AA79
Emel'yanenko, V. V., Asher, D. J., & Bailey, M. E. 2005, MNRAS, 361, 1345
Emery, J. P., Burr, D. M., & Cruikshank, D. P. 2011, AJ, 141, 25
Farkas-Takács, A., Kiss, Cs., Pál, A., et al. 2017, AJ, 154, 119
Fernández, Y. R., Jewitt, D. C., & Sheppard, S. S. 2005, AJ, 130, 308
Fornasier, S., Barucci, M. A., de Bergh, C., et al. 2009, A&A, 508, 457
Gomes, R. S., Soares, J. S., & Brasser, R. 2015, Icar, 258, 37
Guilbert, A., Alvarez-Candal, A., Merlin, F., et al. 2009, Icar, 201, 272
Hapke, B. 1993, Theory of Reflectance and Emittance Spectroscopy (Cambridge: Cambridge Univ. Press)
Ivezić, Ž., Lupton, R. H., Jurić, M., et al. 2002, AJ, 124, 2943
Jester, S., Schneider, D. P., Richards, G. T., et al. 2005, AJ, 130, 873
Jewitt, D. 2005, AJ, 129, 530
Khare, B. H., Thompson, W. R., Sagan, C., et al. 1990, NASCP, 3077, 340
Khare, B. N., Sagan, C., Arakawa, E. T., et al. 1984, Icar, 60, 127
Kiss, C., Szabó, G., Horner, J., et al. 2013, A&A, 555, A3
Lacerda, P., Fornasier, S., Lellouch, E., et al. 2014, ApJL, 793, L2
Lacerda, P., Jewitt, D., & Peixinho, N. 2008, AJ, 135, 1749
Lamy, P. L., Toth, I., Fernandez, Y. R., & Weaver, H. A. 2004, in Comets II, ed. M. C. Festou, H. U. Keller, & H. A. Weaver (Tucson: Univ. Arizona Press), 223
Levison, H. F., & Duncan, M. J. 1997, Icar, 127, 13
Licandro, J., & Pinilla-Alonso, N. 2005, ApJL, 630, L93
Lorenzi, V., Pinilla-Alonso, N., Licandro, J., Dalle Ore, C. M., & Emery, J. P. 2014, A&A, 562, AA85
Luu, X. J. 1993, Icar, 104, 138
Mastrapa, R. M., Sandford, S. A., Roush, T. L., Cruikshank, D. P., & Dalle Ore, C. M. 2009, ApJ, 701, 1347
McComas, D. J., Dayeh, M. A., Funsten, H. O., Livadiotis, G., & Schwadron, N. A. 2013, ApJ, 771, 77
McDonald, G. D., Thompson, W. R., Heinrich, M., Khare, B. N., & Sagan, C. 1994, Icar, 108, 137
Meech, K. J., & Belton, M. J. S. 1989, IAU Circ. No. 4770, ed. D. W. E. Green (Cambridge: Cambridge Univ. Press), 1
Munari, U., Sordo, R., Castelli, F., & Zwitter, T. 2005, A&A, 442, 1127
Perna, D., Barucci, M. A., Fornasier, S., et al. 2010, A&A, 510, A53
Pinilla-Alonso, N., Brunetto, R., Licandro, J., et al. 2009, A&A, 496, 547
Pinilla-Alonso, N., Licandro, J., Gil-Hutton, R., & Brunetto, R. 2007, A&A, 468, L25
Pinilla-Alonso, N., Alvarez-Candal, A., Melita, M. D., et al. 2013, A&A, 550, A13
Protopapa, S., Grundy, W. M., Reuter, D. C., et al. 2017, Icar, 287, 218
Rabinowitz, D., Schwamb, M. E., Hadjiyska, E., Tourtellotte, S., & Rojo, P. 2013, AJ, 146, 17
Rouleau, F., & Martin, P. G. 1991, ApJ, 377, 526
Shkuratov, Y., Starukhina, L., Hoffmann, H., & Arnold, G. 1999, Icar, 137, 235
Szabó, Gy. M., Ivezić, Ž., Jurić, M., Lupton, R., & Kiss, L. L. 2004, MNRAS, 348, 987
Szabó, G. M., Kiss, L. L., Pál, A., et al. 2012, ApJ, 761, 8
Tiscareno, M. S., & Malhotra, R. 2003, AJ, 126, 3122